Thermochimica Acta 518 (2011) 82–88

Contents lists available at ScienceDirect

Thermochimica Acta

journal homepage: www.elsevier.com/locate/tca

An overall numerical investigation on heat and mass transfer for miniature flat plate capillary pumped loop evaporator

Z.M. Wan[a,*], J. Liu[a], J.H. Wan[a], Z.K. Tu[b], W. Liu[b]

[a] Department of Physics, Hunan Institute of Science and Technology, Yueyang, Hunan 414006, PR China
[b] School of Energy and Power Engineering, Huazhong University of Science and Technology, Wuhan 430074, PR China

ARTICLE INFO

Article history:
Received 3 June 2010
Received in revised form 26 January 2011
Accepted 9 February 2011
Available online 24 February 2011

Keywords:
Capillary pumped loop
Thermal management
Heat and mass transfer
Numerical analysis

ABSTRACT

Two-dimensional mathematical model of the miniature flat plate capillary pumped loop (CPL) evaporator is presented to simulate heat and mass transfer in the capillary porous structure and heat transfer in the vapor grooves and metallic wall. The overall evaporator is solved with SIMPLE algorithm as a conjugate problem. The shape and location of vapor–liquid interface inside the wick are calculated and the influences of applied heat fluxes, liquid subcooling and metallic wall materials on the evaporator performances are discussed in detail. The effect of heat conduction of side metallic wall on the performance of miniature flat plate CPL evaporator is also analyzed, and side wall effect heat transfer limit is introduced to estimate the heat transport capability of capillary evaporator. The conjugate model offers a numerical investigation in the explanation of the robustness of the flat plate CPL operation.

1. Introduction

In the developments of the small spacecraft in the space industry, thermal control requirements to such systems have certainly outgrown the capability of conventional single-phase systems and heat pipes in terms of heat transport, heat density, transfer heat distance, and temperature control [1,2] The capillary pumped loop (CPL) is a two-phase thermal control device, which has been advanced in recent twenty years. As a derivative of the heat pipe, CPL is capable of transporting large heat density and passively transporting heat over large distances with minimal temperature differences, and uses capillary action for fluid transport and contains no moving parts. Moreover heat is transferred along with evaporation and condensation, a CPL is much more economical in terms of weight than conventional heat systems [3,4]. Therefore, miniature CPL is especially well suited for thermal management in small spacecraft [5], and because flat plate evaporator has the advantages of good contact condition, low thermal resistance and isothermal heated surface, our primary interest in this investigation is miniature flat plate CPL.

As shown in Fig. 1, a generic miniature flat plate CPL consists of an evaporator, a condenser, a reservoir, vapor and liquid transport lines. Detailed descriptions of working principle of CPL can be found in Nakayama et al. [6]. The capillary evaporator is the most important part in a CPL system because it is the heat absorbing element and provides the capillary force of fluid through the loop. Consequently, the optimal design of CPL requires a thorough understanding of physical behaviors occurring inside the evaporator.

Cao and Faghri [7] developed an analytical solution for heat and mass transfer processes during evaporation in the wick of a CPL evaporator. In this study, it was assumed that the entire porous structure was saturated with liquid and the liquid–vapor interface was located on the unheated portion of the upper surface. Demidov and Yatsenko[8] presented a numerical study showing that vapor zones can take place within the wick in the capillary evaporator under the fins. Figus et al. [9] have also presented a numerical solution for heat and mass transfer in the cylindrical evaporator wick by using the Darcy model and a two-dimensional pore network model. Yan and Ochterbeck [10] provided a numerical study on the flow and heat transfer in the wick of evaporator based on two-phase mixture model. In these works mentioned above, the computational domain is a single segment of wick structure in the evaporator. However, as shown in Fig. 2, the evaporator consists of wick, metallic wall, vapor and liquid grooves. The computational domain mentioned above is only a very small part of wick, and it leads to some shortages in evaluating the overall evaporator performance by these models. Firstly, these models can not predict the influences of metallic wall, vapor grooves and liquid grooves on heat and mass transfer of the evaporator, the heated surface temperature which is very important in estimating the performance of thermal management system can not obtained, too. Secondly, the heat conduction of metallic wall is not considered, especially for a miniature flat plate evaporator. Due to the high thermal conductivity of metallic wall, the liquid inside the bottom of wick and the

* Corresponding author. Tel.: +86 730 8713099; fax: +86 730 8640052.
E-mail address: zhongminwan@hotmail.com (Z.M. Wan).

0040-6031/$ – see front matter © 2011 Elsevier B.V. All rights reserved.
doi:10.1016/j.tca.2011.02.010

Nomenclature

C	specific heat [J Kg^{-1} °C^{-1}]
k	thermal conductivity [W m^{-1} °C^{-1}]
T	temperature [°C]
t	time [s]
$\vec{V}$	velocity vector [m s^{-1}]
P	pressure [Pa]
ΔP_c	capillary force [Pa]
K	permeability [m^2]
L_x	total length in x-direction [m]
L_{x1}	thickness of side metallic wall [m]
L_y	total length in y-direction [m]
L_{y1}	height of the bottom metallic wall [m]
L_{y2}	height of the upper surface of wick [m]
$L_{w\text{-}l}$	length of wick–liquid grooves border [m]
q	heat flux [W m^{-2}]
u	velocity in x-direction [m s^{-1}]
v	velocity in y-direction [m s^{-1}]
h_{fg}	latent heat of evaporation [J kg^{-1}]
r_e	effective capillary radius of wick porous [m]
A	area [m^2]

Greek symbols

μ	viscosity [Pa s]
ρ	density [Kg m^{-3}]
ε	porosity [%]
σ	liquid–vapor surface tension [N m^{-1}]
θ	effective contact angle [°]

Subscripts

mw	metallic wall
eff	effective
l	liquid
s	solid
v	vapor
in	inlet
sat	saturation
sub	subcooling
sup	superheating
a	ambient
i	l, v

liquid grooves may possibly heat up to a temperature that is greater than the saturation temperature corresponding to local saturation pressure by heat conduction of metallic side wall, vapor potentially may generate there as well, and vapor presence in there has been found to fully or partially block liquid flow to the vapor–liquid interface [11], which may lead eventually to dry-out of an evaporator and failure of CPL system. Therefore, the entire model is indispensable for complete understanding of the behavior of the capillary evaporator.

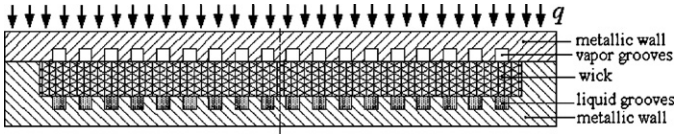

Fig. 2. Schematic of miniature flat plate evaporator.

In the present work, an overall evaporator model of miniature flat plate CPL which couples liquid and vapor flow, heat transfer and phase change in the porous wick and heat transfer in the vapor grooves and metallic wall is presented. The entire evaporator is solved numerically with SIMPLE algorithm as a conjugate problem. The entire evaporator model can predict the influences of metallic wall, vapor grooves and liquid grooves on heat and mass transfer of the capillary evaporator, and the influence of heat conduction of metallic side wall on the performance of evaporator is considered and the temperature levels of heated surface can be gotten. Furthermore, the entire model is able to completely forecast physical process in the CPL evaporator, and the heat transfer capacity and the reliability of CPL system can be predicted by the model. To the best of our knowledge, the entire evaporator model has not been proposed before in the context of capillary evaporators.

2. Mathematical model

As the evaporator is taken to be symmetric, a half of evaporator cross section is selected as the computational domain, as shown in Fig. 3.

To develop the mathematical model, the main assumptions are made as follows:

(1) For simplicity, the vapor flow in the vapor grooves is neglected, and heat transfer is mainly by conduction.
(2) The porous media is rigid, homogenous, isotropic and fully saturated with fluid. There is local thermodynamic equilibrium between solid phase and fluid phase, and the fluid is incompressible and has constant property.
(3) The liquid in the liquid grooves comes from the condenser directly, and the temperatures in these regions are equal to liquid inlet temperature.

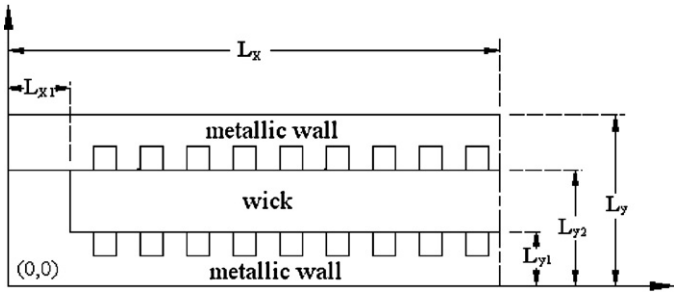

Fig. 3. Computation domain and coordinate system.

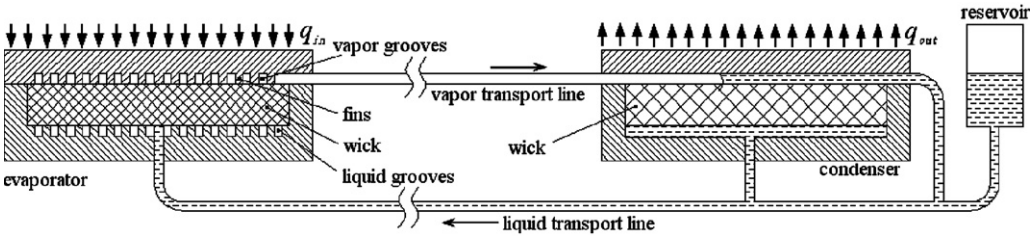

Fig. 1. Schematic of a miniature flat-plate CPL system.

For the space environment, the effect of gravity is neglected. Figus et al. [9] have developed the continuum model and discrete model of porous media to investigate the heat and mass transfer in the porous media and the assumption of zero thickness for the two-phase zone were given, and their theoretical results are credible. In the present work, the assumption of zero thickness for the two-phase zone is used to simplify model of the wick. The heat and mass transfer for the liquid and vapor regions in the wick structure are based on the volume-averaged technique and Brinkman–Darcy–Forchheimer model of porous media.

Governing equations:

(1) Metallic wall:

$$(\rho c)_{\mathrm{mw}}\frac{\partial T}{\partial t}=k_{\mathrm{mw}}\left(\frac{\partial^2 T}{\partial x^2}+\frac{\partial^2 T}{\partial y^2}\right) \tag{1}$$

(2) Vapor grooves:

$$(\rho c)_{\mathrm{v}}\frac{\partial T}{\partial t}=k_{\mathrm{v}}\left(\frac{\partial^2 T}{\partial x^2}+\frac{\partial^2 T}{\partial y^2}\right) \tag{2}$$

(3) Wick structure

Continuum equation:

$$\frac{\partial(\varepsilon_i\rho_i)}{\partial t}+\nabla\cdot(\rho_i\vec{V}_i)=0 \tag{3}$$

Momentum equation:

$$\frac{\rho_i}{\varepsilon_i}\frac{\partial\vec{V}_i}{\partial t}+\frac{\rho_i}{{\varepsilon_i}^2}\nabla(\vec{V}_i\cdot\nabla)\vec{V}_i=-\nabla p-\left(\frac{\mu_i}{K}+\frac{C|\vec{V}_i|}{\sqrt{K}}\right)\vec{V}_i+\frac{\mu_i}{\varepsilon_i}\nabla^2\vec{V}_i \tag{4}$$

Energy equation:

$$\overline{(\rho c)}_i\frac{\partial T}{\partial t}+\rho_i c_i(\vec{V}_i\cdot\nabla)T=(k_{\mathrm{eff}})_i\nabla^2 T \tag{5}$$

(4) Liquid grooves

$$T=T_{\mathrm{in}} \tag{6}$$

where i = l, v; C is the Forchheimer's constant; n is the normal unit vector at the vapor–liquid interface; (k_{eff}) is the effective thermal conductivity, $(k_{\mathrm{eff}})_i=\varepsilon k_i+(1-\varepsilon)k_{\mathrm{s}}$; $\overline{(\rho c)}$ is the density–capacity heat product defined in the energy equations, $(\overline{\rho c})_i=\varepsilon\rho_i c_i+(1-\varepsilon)\rho_{\mathrm{s}}c_{\mathrm{s}}$.

The mathematical model includes several parts, which consist of metallic wall, vapor grooves, wick structure and liquid grooves. The geometrical configuration between parts is shown in Fig. 2, and flow and heat transfer between two parts are coupling. The conjugate boundary conditions exist at the interface of two regions. The heat flux and temperatures should be continuous at the interface on both sides.

Boundary conditions:

At $x=0$:

$$k_{\mathrm{mw}}\frac{\partial T}{\partial x}=0 \tag{7}$$

At $x=L_x$:

$$\frac{\partial T}{\partial x}=0 \tag{8}$$

At $y=0$:

$$k_{\mathrm{mw}}\frac{\partial T}{\partial y}=0 \tag{9}$$

At $y=L_y$:

$$k_{\mathrm{mw}}\frac{\partial T}{\partial y}=q \tag{10}$$

Due to fluid flow occurring inside the wick, the boundary conditions of momentum equations are as follows:

At $y=L_{y1}$ and $L_{x1}\le x\le L_x$:

$$u_{\mathrm{l}}=0,\ v_{\mathrm{l}}=0\quad\text{wick-bottom wall border} \tag{11}$$

$$u_{\mathrm{l}}=0,\ v_{\mathrm{l}}=v_{\mathrm{in}}\quad\text{wick-liquid grooves border} \tag{12}$$

At $y=L_{y2}$ and $L_{x1}\le x\le L_x$:

$$\frac{\partial v_{\mathrm{v}}}{\partial y}=0,\ \frac{\partial u_{\mathrm{v}}}{\partial x}+\frac{\partial v_{\mathrm{v}}}{\partial y}=0$$

wick-vapor grooves border in vapor phase region (13)

$$u_i=0,\ v_i=0\quad\text{other border},\ i=v,l \tag{14}$$

At $x=0$ and $L_{y1}\le y\le L_{y2}$:

$$u_i=0,\ v_i=0\quad i=v,1 \tag{15}$$

At $x=L_x$ and $L_{y1}\le y\le L_{y2}$:

$$u_i=0,\ \frac{\partial v_i}{\partial x}=0 \tag{16}$$

The inlet liquid velocity v_{in} in Eq. (12) at the wick–liquid grooves border can be obtained by performing a overall energy balance on the capillary evaporator.

$$v_{\mathrm{in}}=\frac{qA_x}{\rho_{\mathrm{l}}A_{\mathrm{in}}(h_{\mathrm{fg}}+c_{\mathrm{l}}\Delta T_{\mathrm{sub}}+c_{\mathrm{v}}\Delta T_{\mathrm{sup}})} \tag{17}$$

Sharp discontinuities of the fluid properties appear across vapor–liquid interface, but continuities of the mass and heat flux should be maintained there.

Mass continuity condition:

$$\rho_{\mathrm{l}}\vec{V}_{\mathrm{l}}=\rho_{\mathrm{v}}\vec{V}_{\mathrm{v}} \tag{18}$$

Energy conservation condition:

$$(k_{\mathrm{eff}})_v\nabla T_{\mathrm{v}}\cdot n-(k_{\mathrm{eff}})_{\mathrm{l}}\nabla T_{\mathrm{l}}\cdot n=\rho_{\mathrm{l}}|\vec{V}_{\mathrm{l}}|h_{\mathrm{fg}} \tag{19}$$

Temperature continuity condition:

$$T_{\mathrm{l}}=T_{\mathrm{v}}=T_{\mathrm{sat}} \tag{20}$$

As evaporation takes place inside the wick structure, the capillary menisci is established at the vapor–liquid interface and capillary pressure is developed, which circulates the fluid throughout the CPL.

$$\Delta P_{\mathrm{c}}=P_{\mathrm{v}}-P_{\mathrm{l}}=\frac{2\sigma\cos\ \theta}{r_{\mathrm{e}}} \tag{21}$$

Eq. (20) presents the local thermal equilibrium at the vapor–liquid interface inside the wick structure, and the saturation temperature T_{sat} is equal to the setpoint temperature of two-phase reservoir of CPL. This condition is used to determine the location of vapor–liquid interface. Because the maintenance of a continuous flow of fluid is assured by the capillary pressure of wick, ΔP_{c} in Eq. (21) should be equal to the total pressure loss in the CPL loop.

3. Numerical procedure

The finite difference method is used in the numerical procedure and the governing equations together with the boundary conditions in the different regions of the evaporator are solved as a conjugate problem with the SIMPLE algorithm [12]. The mathematic model can predict the transient characteristics of evaporator,

but the steady-state results are only discussed in this work. Conjugate problem includes liquid and vapor flow, heat transfer and phase change in the porous wick structure and heat transfer in the fluid region and metal wall, and these increase the complication of numerical procedure significantly. The additional difficulty here is that the location of the vapor–liquid interface involving phase change is not known. An interface tracking method which is based on the moving structured grid is used to locate the vapor–liquid interface. The numerical technique for solid zone inside the computation domain has been described in detailed in Ref. [13], and it has not represented any more here. The overall numerical sequence is described as follows:

(1) Initialize the problem, and choose an initial arbitrary vapor–liquid location inside the wick.
(2) Generate the structured grid inside the wick.
(3) Solve the continuum and momentum equations separately in the vapor and liquid regions inside the wick.
(4) Regenerate grid inside the entire evaporator.
(5) Solve the energy equations for all regions inside overall evaporator.
(6) Check whether the temperature condition at the interface is satisfied. If it is not satisfied, the vapor–liquid interface location has to be updated.
(7) Go back to step (2) until convergence.

When the vapor–liquid interface is modified at the step (6), the pressure drop across the interface is computed to ensure it is less than the maximum capillary pressure in the wick $P_v - P_l \leq \frac{2\sigma}{r_e}$

The convergence criteria of the numerical solution for velocity, pressure and temperature are that relative errors between two consecutive iterations are less than 10^{-6}.

4. Results and discussions

Numerical results are determined with methanol as the working fluid. The thermal properties taken in the computation are: $k_l = 0.202\,W\,m^{-1}\,K^{-1}$, $k_v = 0.0139\,W\,m^{-1}\,K^{-1}$, $\mu_i = 5.2 \times 10^{-4}\,N\,s^{-1}\,m^{-2}$, $\mu_v = 1.07 \times 10^{-5}\,N\,s^{-1}\,m^{-2}$, and $h_f = 1.12 \times 10^{6}\,J\,kg^{-1}$. The sintered stainless steel wick is used as the wick structure, the properties for the wick structure are: $k_s = 15.2\,W\,m^{-1}\,K^{-1}$, $\varepsilon = 0.611$, and $K = 6.616 \times 10^{-13}\,m^2$. Here copper and stainless steel are chosen as the material of metallic wall, since they are compatible with methanol. The geometric parameters of the evaporator are: $L_x = 21.5 \times 10^{-3}$ m, $L_{x1} = 3 \times 10^{-3}$ m, $L_y = 10 \times 10^{-3}$ m, $L_{y1} = 3 \times 10^{-3}$ m, and $L_{y2} = 7 \times 10^{-3}$ m. Both length and height of vapor and liquid grooves are 0.5×10^{-3} m. The two-phase reservoir of CPL system is used to control the temperature of the loop and accommodates fluid inventory shifts during changes in operating conditions, and the setpoint temperature of reservoir is the liquid saturated temperature T_{sat}, which is the temperature of vapor–liquid interface. The setpoint temperature is 35 °C, which is the liquid saturated temperature T_{sat}. The grid schemes of global evaporator are 237×82.

Fig. 4 shows the velocity vectors for the liquid phase in the wick (x range from 3 mm to 12.5 mm), and the magnitude of liquid velocity is $10^{-5}\,m\,s^{-1}$. As seen, the wick structure contains vapor region under the fins separated from the liquid region by the vapor–liquid interface. The shape of vapor–liquid interface is wavy near the upper surface of wick, and the vapor region is very small. Because of the zero thickness of vapor–liquid interface for the porous wick fully saturated with fluid, the evaporation and liquid vapor transition only occur at the interface, and the liquid velocity is nearly uniform in most liquid zone except near the wick borders. Fig. 4 also shows that the liquid evaporation mostly takes place near the upper surface of wick structure, and at the same time, because of heat conduction of side metallic wall, the liquid evaporation occurs in the vicinity of upper left-hand surface, too. Since the vapor zone is very small, the vapor velocity vectors are not given in this paper.

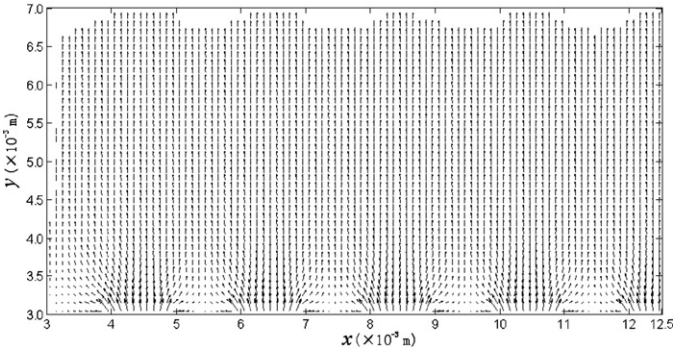

Fig. 4. Liquid velocity vectors in the wick structure (copper wall, $q = 3 \times 10^4\,W\,m^{-2}$, $\Delta T_{sub} = 3\,°C$).

Fig. 5 shows the temperature fields of the evaporator with different heat fluxes. The heat load imposed on the outer surface of the evaporator is transferred to wick in two ways: (1) through the metallic fins and (2) through the vapor grooves. Because of great difference in thermal conductivity between the metallic fins and vapor, the heat is transferred to wick mainly by conduction of the fins, and the shape of isothermal lines near the upper surface of wick structure is wavy. The shape of vapor–liquid interface where the temperature contour level is equal to the saturated temperature inside the wick is also wavy, and it is determined by the geometric parameters of fins and vapor grooves. Naturally, the thin gaps between the fins and upper surface of wick saturated by vapor appear, these gaps allow the vapor to escape from the wick. The vapor–liquid interface locates near the upper and left surface of wick, as has been observed by the visualization experiment of Zhao et al. [14]. When the heat flux is increased, the vapor–liquid interface inside the wick moves away from the fins and the size of the vapor zone and the gaps enlarges, it can be found in Fig. 5.

Since the thickness of side metallic wall cannot be negligible for the miniature flat plate evaporator, the influence of heat conduction of side metallic wall on heat transport capacity needs to be investigated. At low heat flux, as seen in Fig. 5(a), the left vapor–liquid interface locates near the upper left-hand surface of wick, this means that liquid evaporation takes place there and it is safe for CPL normal operation. With the increases of heat flux, the influence heat conduction of side metallic wall on the vapor–liquid interface is very significant, as shown in Fig. 5(b) and (c). It can be seen that the left vapor–liquid interface has gone deeply to the bottom of wick, even to the liquid groove. This indicates that the vapor formation in the bottom of wick and even in the liquid groove under these conditions, and the vapor presence in there can fully or partially block liquid to vapor–liquid interface to evaporate and result eventually in dry-out of the evaporator. For a miniature flat plate CPL evaporator, the heat conduction of side metallic wall leads to the day-out of evaporator, this is considered as a heat transfer limit, called side wall effect heat transfer limit here, which is a very important heat transfer limit compared to other heat transfer limits, and this is great difference between miniature flat plate CPL and cylindrical CPL.

Fig. 6 presents the influence of inlet liquid subcooling on the temperature of global evaporator. As shown in Fig. 6, it can be found that increasing the inlet liquid subcooling increases the temperature gradients inside the wick structure. Naturally, the temperature difference between the upper surface and bottom surface of wick increases with increasing liquid subcooling, this increase of tem-

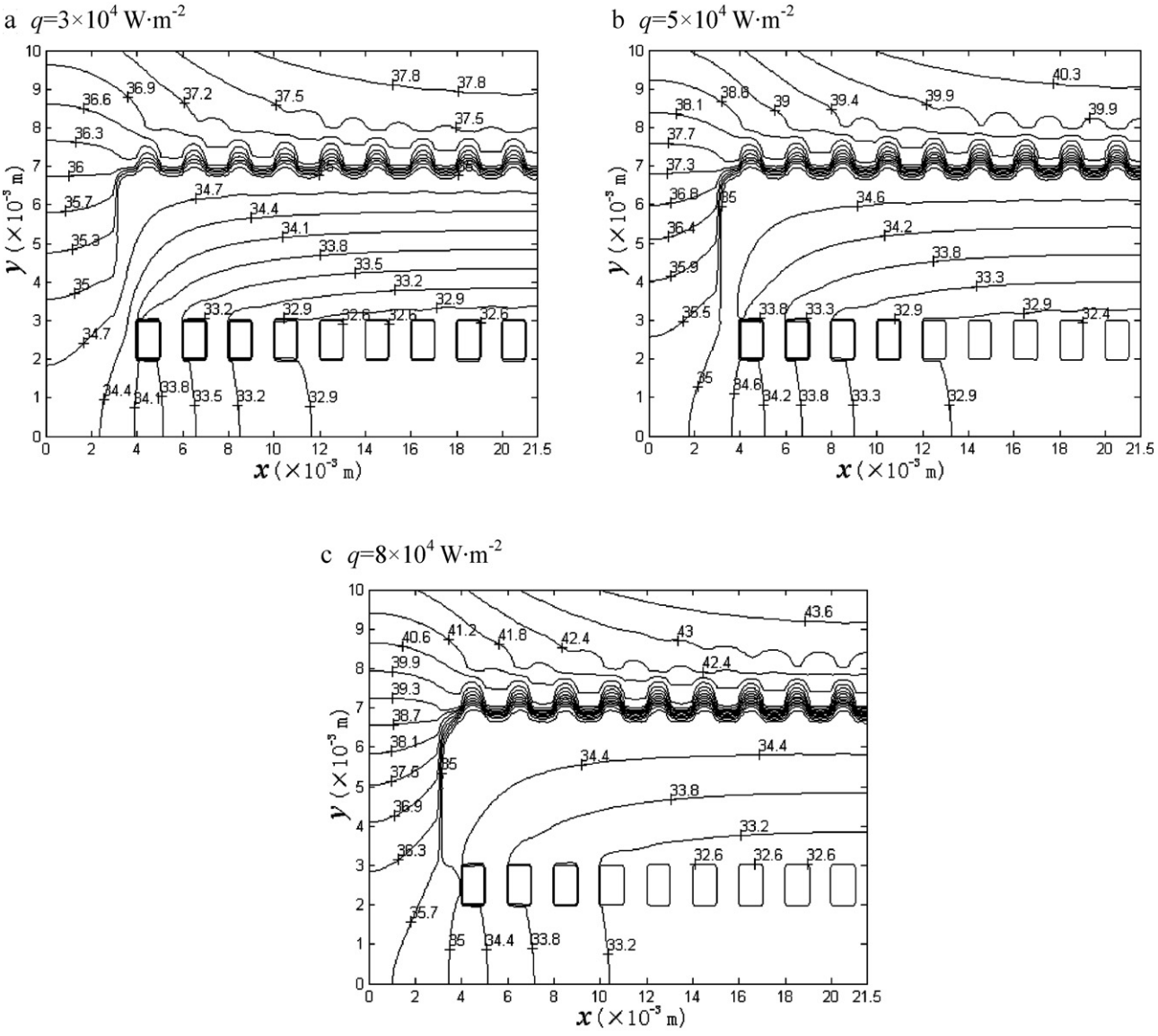

Fig. 5. Temperature fields in the evaporator (copper wall, ΔT_{sub} = 3 °C). (a) $q = 3 \times 10^4$ W m^{-2}, (b) $q = 5 \times 10^4$ W m^{-2} and (c) $q = 8 \times 10^4$ W m^{-2}.

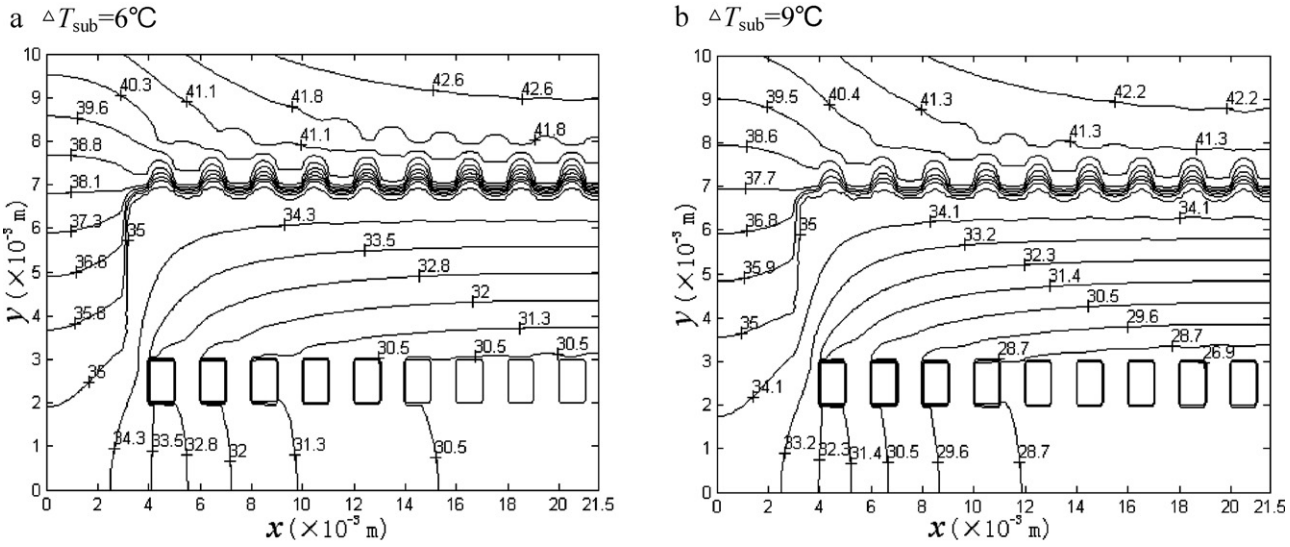

Fig. 6. Temperature fields in the evaporator (copper wall, $q = 8 \times 10^4$ W m^{-2}). (a) ΔT_{sub} = 6 °C, and (b) ΔT_{sub} = 9 °C.

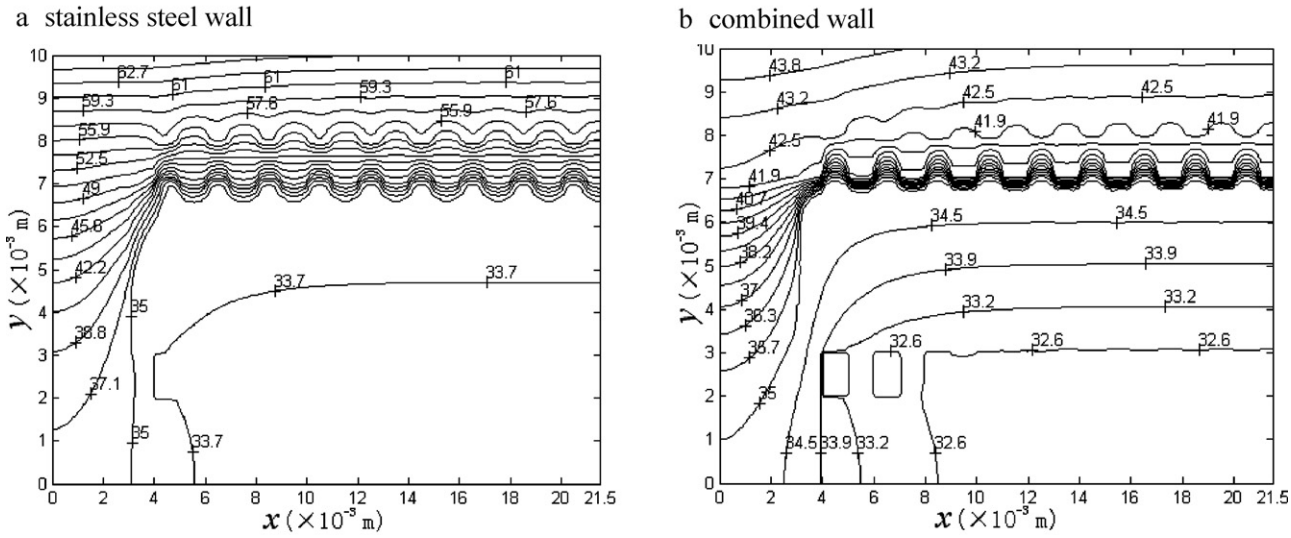

Fig. 7. Temperature fields in the evaporator ($\Delta T_{sub} = 3\,^{\circ}C$, $q = 8 \times 10^4\,W\,m^{-2}$). (a) Stainless steel wall, and (b) combined wall.

perature difference aids in preventing vapor formation in the liquid grooves and inside the bottom wick, and it helps to increase the safety of CPL. Furthermore, As seen from Figs. 5(c) and 6, at the low liquid subcooling of 3 °C, the left vapor–liquid interface has invaded deeply into the liquid groove, and it indicates that evaporator has nearly reached its side wall effect heat transfer limit. But at the high liquid subcooling of 6 °C and 9 °C, the vapor–liquid interface locates near the wick-side wall border, not goes deep into liquid groove, and the CPL can operate safely. As a result, increasing the liquid subcooling can enhance the side wall effect heat transfer limit of the evaporator.

In order to investigate the effects of wall material on the performance of evaporator, stainless steel wall and combined wall (upper wall material is copper, side and bottom wall material is stainless steel) are also used in the computation. Fig. 7 shows the temperature distributions in the evaporator with stainless steel wall and combined wall at $\Delta T_{sub} = 3\,^{\circ}C$ and $q = 8 \times 10^4\,W\,m^{-2}$. Because of low thermal conductivity for stainless steel wall, the temperature gradient is very large in the upper wall zone, and decreases in the wick and bottom wall zone. It is very clear to find that most of applied heat load has been used for the liquid evaporation near the upper and left surface of wick. For the cases of copper wall and combined wall, Because of high thermal conductivity, the temperature gradient is small in the upper wall zone. From Fig. 5(c), it can see that the vapor–liquid interface has gone deeply into the liquid groove, naturally, the evaporator has almost reached its side wall effect heat transfer limit. But as seen from Fig. 9, the vapor–liquid interfaces have not invaded deeply into the grooves at the same heat flux, which indicated that the evaporator with stainless steel or combined wall has higher side wall effect heat transfer limit.

The heated surface of the evaporator is attached to the apparatus which needs cooling, and high temperatures of heated surface may result in abnormality of the apparatus. Consequently, the temperature level of heated surface is a very important parameter to estimate the performance of CPL evaporator.

Fig. 8 shows the heated surface temperatures along x direction for different wall materials at $q = 8 \times 10^4\,W\,m^{-2}$. As seen, the heated surface temperature of evaporator with stainless steel wall is more than 65 °C, and it is dangerous to the normal operation of cooled apparatus. But the heated surface temperatures with copper wall and combined wall are less than 45 °C, it is moderate for the cooled apparatus, and the cooled apparatus can operate normally under

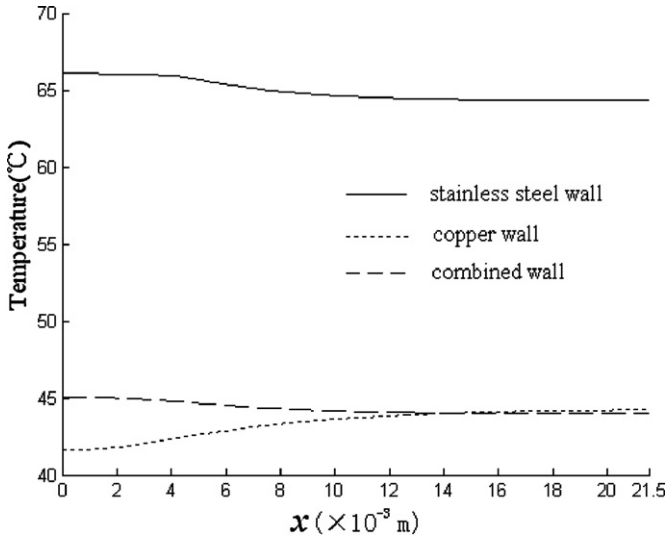

Fig. 8. Temperature profiles on the heated surface ($\Delta T_{sub} = 3\,^{\circ}C$, $q = 8 \times 10^4\,W\,m^{-2}$).

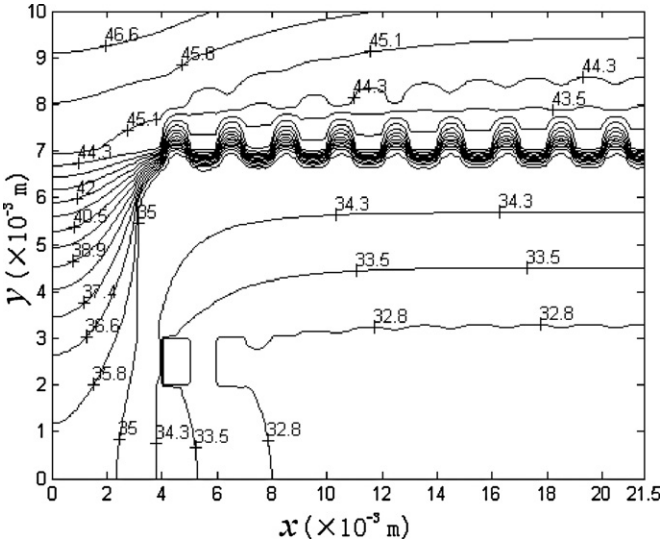

Fig. 9. Temperature fields in the evaporator ($\Delta T_{sub} = 3\,^{\circ}C$, $q = 10 \times 10^4\,W\,m^{-2}$).

these conditions. Thereby, the thermal conductivity of wall has a significant influence on the heated temperature, and the upper metallic wall with high thermal conductivity results in low heated surface temperature.

To decrease the temperatures of the heated surface and increase the side wall effect heat transfer limit of miniature flat plate CPL evaporator, the combined wall should be chosen for dissipating high heat fluxes. Fig. 9 shows the temperature distribution in the evaporator at $q = 10 \times 10^4\ W\,m^{-2}$, as seen, the vapor–liquid interface has not gone deeply into the liquid grooves, and thus the evaporator has not reached the side wall effect heat transfer limit. At the same time, the maximal temperature of heated surface is about 47.5 °C, which is moderate for cooling of electronic devices. Therefore, the miniature flat plate evaporator with combined wall can improve the heat transport capacity and maintain an appropriate temperature level of the heated surface.

5. Conclusions

A two-dimensional model for the global evaporator of miniature flat CPL evaporator is developed, and the governing equations for different zones are solved numerically as a conjugate problem using the SIMPLE algorithm.

The liquid evaporation occurs in the vicinity of upper and left surface of wick structure, and the location and shape of vapor–liquid interface are mainly affected by the heat fluxes and geometric parameters of fins and vapor grooves. With the increases of the applied heat fluxes, the vapor–liquid interface inside the wick moves away from the fins and the size of the vapor zone enlarges. The side wall effect heat transfer limit is introduced to estimate the heat transport capability of the miniature flat plate evaporator, and it is a very important heat transfer limit compared to others. Increasing the inlet liquid subcooling can increase the temperature difference between the upper and bottom surface of wick, and thus helps to prevent the vapor formation in the liquid grooves and the bottom wick, as well as increase heat transport capacity of the evaporator. The evaporator with single aluminum wall results in low side wall effect heat transfer limit, but leads to low temperature level of the heated surface. On the other hand, the evaporator with single stainless steel wall leads to higher heat transport capacity, but to higher temperature level of the heated surface. The evaporator with combined wall can greatly increase side wall effect heat transfer limit and maintain an appropriate temperature level on the heated surface, which imply that the CPL can operate safely and cooled apparatus can also work effectively under higher heat fluxed.

The present overall numerical model of miniature flat plate CPL evaporator can effectively estimate the heat transfer capacity of evaporator and evaluate the temperature level of the heated surface, and it is useful for the evaporator design and performance optimization of miniature flat plate CPL.

Acknowledgements

The current work is supported by the National Key Basic Research Development Program of China (No. 2007CB206901), China Postdoctoral Science Foundation (20090451038) and Scientific Research Fund of Hunan Provincial Education Department (09B041).

References

[1] J. Wukchul, H. Hyungjin, J. Lee, International Journal of Heat and Mass Transfer 53 (2010) 268–275.
[2] R. Nadalini, F. Bodendieck, Acta Astronautica 58 (2006) 564–575.
[3] H.W. Lin, W.K. Lin, Thermal Engineering 29 (2009) 186–194.
[4] Z.C. Liu, W. Liu, J.G. Yang, Journal of Thermophysics and Heat Transfer 22 (2008) 98–104.
[5] P.C. Gian, C. Maurizio, F. Massimo, Experimental Thermal and Fluid Science 34 (2010) 866–878.
[6] Z.C. Liu, W. Liu, A. Nakayama, Heat and mass transfer 43 (2007) 1273–1281.
[7] Y. Cao, A. Faghri, International Journal of Heat and Mass Transfer 37 (1994) 1525–1553.
[8] A.S. Demidov, E.S. Yatsenko, International Journal of Heat and Mass Transfer 37 (1994) 2155–2163.
[9] C. Figus, Y.L. Bray, S. Bories, M. Prat, International Journal of Heat and Mass Transfer 42 (1999) 2557–2569.
[10] Y.H. Yan, J.M. Ochterbeck, Journal of Electronic Packaging 125 (2003) 251–260.
[11] J. Tim, I.M. LaClair, International Journal of Heat and Mass Transfer 43 (2000) 3937–3952.
[12] W.Q. Tao, Numerical Heat Transfer, Xi'an Jiao Tong University Press, Xi'an, China, 2001.
[13] M. Yang, W.Q. Tao, ASME Journal of Heat Transfer 117 (1995) 619–625.
[14] T.S. Zhao, Q. Liao, International Journal of Heat and Mass Transfer 43 (2000) 1141–1155.